

19 March 2012, UW-CPTC 11-13R

Resonant magnetic perturbation effects on pedestal structure and ELMs

J.D. Callen, A.J. Cole,[‡] C.C. Hegna

University of Wisconsin, Madison, WI 53706-1609 USA

E-mail: callen@engr.wisc.edu, <http://homepages.cae.wisc.edu/~callen>

S. Mordijck

College of William and Mary, Williamsburg, VA 23187-8795 USA

R.A. Moyer

University of California-San Diego, La Jolla, CA 92093-0417 USA

Abstract. The plasma transport processes by which externally applied resonant magnetic field perturbations (RMPs) mitigate or suppress edge localized modes (ELMs) in low collisionality tokamak H-mode plasmas are explored. Experimental data from DIII-D indicates the dominant RMP-induced transport occurs at the pedestal top where electron temperature gradient scale lengths increase up to 3 times more than density gradient scale lengths. The increases scale approximately with the square of the strength of the RMPs. Since flow screening is predicted to inhibit magnetic island formation and magnetic stochasticity, a plasma transport model that does not depend on stochasticity is apparently needed. Thus, a basic magnetic-flutter-based cylindrical screw pinch model theory of plasma transport is developed. A key attribute of this new model is that while RMP-induced radial magnetic perturbations can be significantly reduced on rational surfaces by flow screening, they induce spatial magnetic flutter away from them and thereby can cause substantial radial plasma transport. The plasma transport predictions of this spatial flutter model are compared with the DIII-D transport data.

PACS numbers: 52.55.Fa, 52.55.Dy, 52.25.Fi, 52.30.Ex, 52.25.Xz

Submitted to: *Nuclear Fusion*

[‡] Present address: Columbia University, New York, NY 10027 USA

1. Introduction

The desirable high- (H-) modes of plasma confinement in toroidal magnetic systems have large plasma gradients in their edge pedestals (outer few % of the plasma radius). These edge gradients usually increase with time until the ideal magnetohydrodynamic (MHD) peeling-ballooning (P-B) instability criterion [1]–[4] is exceeded and an edge localised mode (ELM [5, 6]) is precipitated. ELMs abruptly and repetitively reduce the edge plasma gradients and deposit intense pulses of hot plasma onto solid materials (usually divertor plates) outside the plasma confinement region. ELMs are particularly problematic [7] for projected high performance fusion plasmas in ITER [8].

Pioneering experiments [9]–[12] in DIII-D have used edge resonant magnetic perturbations (RMPs) to mitigate and often suppress ELMs. As discussed in the next section, in low collisionality ITER-relevant plasmas they do so [11] primarily by reducing the plasma pressure gradient in the vicinity of the top of the H-mode pedestal. The reduced pressure gradient there avoids breaching the P-B instability boundary and precipitating ELMs. Key contributors to reducing the pressure gradient in the RMP-suppressed DIII-D discharges [11] are “density pumpout” in the edge region and a large reduction in the electron temperature gradient at the pedestal top — see section 2. The largest RMP-induced electron temperature changes occur in narrow “resonant” windows [12] of “safety factor” values at the normalized poloidal magnetic flux location $\Psi_N = 0.95$, which is denoted by q_{95} .

The physics of how RMPs reduce the pressure gradient at the pedestal top to suppress ELMs is not presently understood. A working hypothesis [11] is that multiple RMPs induce overlapping magnetic islands in the edge that cause magnetic stochasticity and enhanced plasma transport there. The sensitivity of RMP effects to field line pitch (q_{95}) resonances [9]–[12] and the striated density flux profiles on divertor plates are in qualitative agreement with this model. However, extended MHD modelling [13, 14, 15] usually predicts that extant edge plasma toroidal flows prevent “penetration” of resonant RMP fields and thereby inhibit magnetic reconnection, island formation and stochasticity, particularly at the top of the pedestal where the P-B instability drives may be largest.

This paper develops and tests an alternative theory of the effects of RMPs on low collisionality pedestals. It is based on the enhanced radial plasma transport induced by the three-dimensional (3D) spatial “magnetic flutter” effects [16] of RMPs. In the flutter model the irreversibility needed for plasma transport is produced not by magnetic stochasticity [17] but by electron Coulomb collisions [18]. Small radial magnetic perturbations δB_r can easily modify radial electron heat transport because plasma transport is much faster along magnetic field lines than perpendicular to them. In the flutter model [16] the very large collisional parallel electron thermal diffusivity [18] $\chi_{e\parallel}$ along the RMP-induced 3D field causes a spatially fluttering parallel electron heat flux and consequently a radial electron thermal diffusivity of $\chi_{er}^{\delta B} \sim (\delta B_r/B_0)^2 \chi_{e\parallel}$. Since for pedestal top parameters in DIII-D $\chi_{e\parallel} \rightarrow \chi_{e\parallel}^{\text{ref}} \gtrsim 10^9 \text{ m}^2 \text{ s}^{-1}$ [see Eq. (17) in section 4],

even very small RMP-induced magnetic perturbations ($\delta B_r/B_0 \gtrsim 3 \times 10^{-5}$) can produce additional radial electron thermal diffusivity in excess of the usual experimental level of $\chi_e^{\text{exp}} \sim 1 \text{ m}^2 \text{ s}^{-1}$ [19].

Most previous modelling studies of the plasma response to RMPs [20, 21] have used the four-field reduced MHD model [22, 23] which does not include the parallel electron thermal flux and consequent magnetic flutter effects. A recent study [24] added parallel electron energy transport effects and explored numerically the possible effects on the electron density and temperature profiles in the vicinity of a 2/1 core resonant surface of an externally-imposed single helicity magnetic perturbation. Possible additional effects of drift-wave microturbulence [25] are neglected in this paper because the emphasis here is on electron collisional effects of RMPs on pedestal plasma transport.

This paper is organized as follows. Section 2 presents some key parameters and properties of RMP effects on the electron temperature and density profiles in the edge of DIII-D H-mode plasmas [11]. Particular parameters at $\Psi_N = 0.95$ for a specific DIII-D discharge (#126440) in which RMPs suppress ELMs are discussed there; they will be used to illustrate relevant scale lengths and model predictions in the remainder of the paper. The next section discusses flow screening effects on the RMP-induced magnetic field structure and the resultant RMP effects within the edge plasma. Section 4 develops a cylindrical screw pinch model for the magnetic-flutter-induced electron parallel flow and heat flux, and concomitant radial electron transport caused by RMPs. Section 5 compares the predictions of this model to the DIII-D experimental results presented in section 2. It also discusses this model's key characteristics, what needs to be done to test it further and its possible application to higher collisionality pedestals. The final section summarizes the results and the model's implications for RMP-induced effects on plasma transport in tokamak H-mode pedestals.

2. RMP effects on pedestals in DIII-D

Plasma transport properties for a typical DIII-D H-mode pedestal are discussed in detail in [19]. The effects of RMPs in the plasma edge will be illustrated for the ITER similar shape (ISS) low collisionality discharges in Ref. [11]. Plasma profiles of the electron density n_e and temperature T_e , and ion temperature T_i , and their gradients for this set of discharges with RMP-inducing I-coil currents of 0.0, 4.0, 4.8, 5.2, 5.8 and 6.2 kA are described in Ref. [26]. The radial coordinate used in displaying the profiles there and the remainder of this paper is the normalized poloidal magnetic flux: $\Psi_N \equiv \psi_p/\psi_p(\text{sep})$, which is zero at the magnetic axis and unity at the separatrix.

Figures 1 and 2 show the electron density and temperature profiles before and after RMPs are applied to an ISS plasma in DIII-D [11] by an I-coil current of 5.2 kA. Several features of the changes in the n_e and T_e profiles induced by the RMPs are noteworthy: 1) in the steep gradient region near the separatrix (i.e. for $0.975 \lesssim \Psi_N \lesssim 1$) the RMPs reduce (the magnitude of) the n_e gradient but increase the T_e gradient, 2) the largest RMP-induced decreases in the n_e , T_e gradients occur in the pedestal top

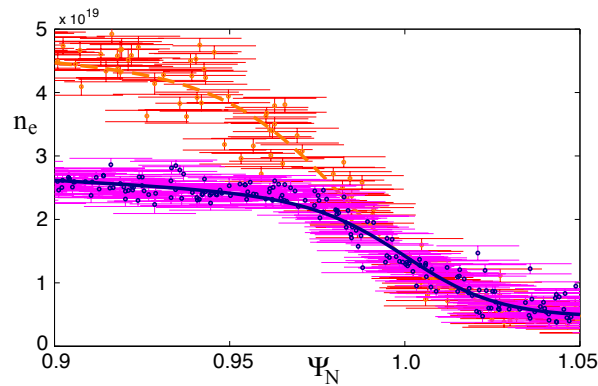


Figure 1. Electron density tanh fit [28] profiles without (dashed, orange) and with (solid, purple) RMPs applied by a 5.2 kA I-coil current. The dots represent individual Thomson scattering data points and the associated thin lines their relevant error bars.

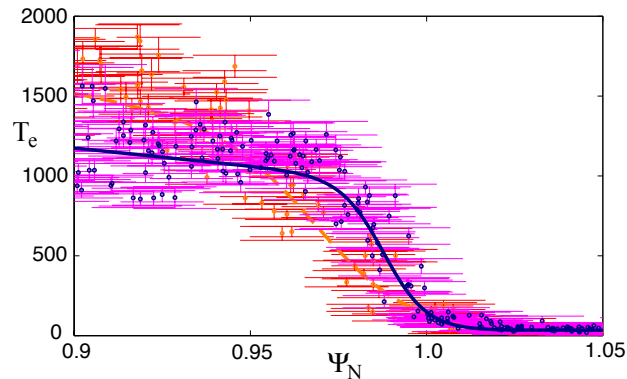


Figure 2. Electron temperature tanh fit [28] profiles without (dashed, orange) and with (solid, purple) RMPs applied by a 5.2 kA I-coil current. The dots represent individual Thomson scattering data points and the associated thin lines their relevant error bars.

region ($0.94 \lesssim \Psi_N < 0.975$), and 3) the n_e , T_e gradients are not changed much as one moves towards the core region ($\Psi_N \lesssim 0.9$).

These features are illustrated directly in Fig. 3 which plots the ratios of electron density n_e and temperature T_e gradient scale lengths with RMPs to those without them. The error bars on the n_e gradient scale lengths have been estimated to be less than 10% [27] and are likely similar for the T_e gradient scale lengths. The RMP-induced increase in the density gradient scale length $L_n \equiv -[d \ln n_e / d\rho]^{-1}$ (decrease of the electron density gradient) throughout the edge region is indicative of the “density pumpout” that is usually induced by RMPs in low collisionality DIII-D plasmas [11]. The variable $\rho \equiv \sqrt{\psi_t / \pi B_0}$ is the toroidal-magnetic-flux-based radial coordinate. The RMP-induced increase in the T_e gradient scale length $L_{T_e} \equiv -[d \ln T_e / d\rho]^{-1}$ (decrease in the T_e gradient) is even larger throughout most of the edge — except for $\Psi_N \gtrsim 0.984$ where it actually decreases (i.e. T_e profile steepens). Note that as Ψ_N decreases toward

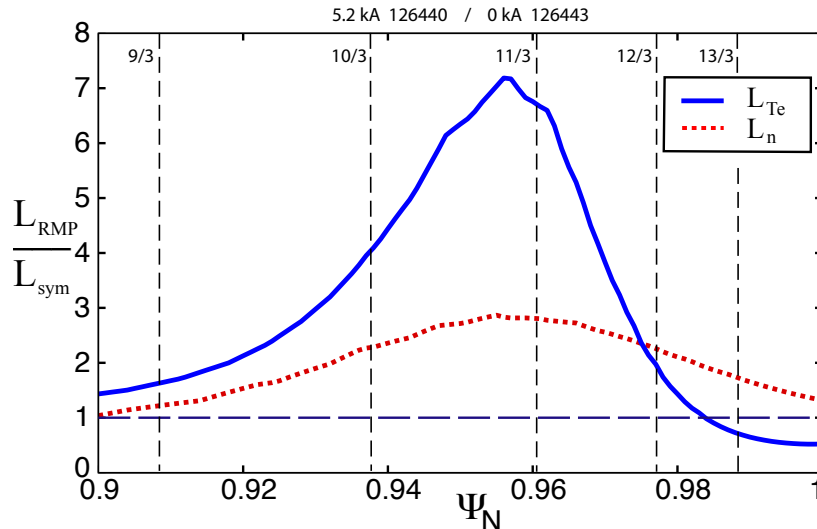


Figure 3. Ratios of electron temperature (solid blue line) and density (dashed red line) gradient scale lengths with RMPs (subscript RMP) to without (subscript sym) induced by a 5.2 kA I-coil current. The radial position of the $q = m/n$ surfaces for DIII-D discharge # 126440 are indicated by the m/n -labeled vertical dashed lines.

0.9 the gradient scale length ratios approach unity. This indicates a transition to the core plasma where the RMPs cause much smaller changes.

In the pedestal top region ($0.94 \lesssim \Psi_N < 0.975$) the increases in the T_e gradient scale lengths are up to about three times the n_e gradient scale length changes. In contrast, in the steep gradient region of the pedestals ($0.975 \lesssim \Psi_N \lesssim 1$) the changes in the gradient scale lengths are quite different — L_{T_e} decreases while L_n increases and L_{T_e} becomes about $1/3$ of L_n . These inverse relationships between the T_e and n_e gradient scale length changes induced by RMPs at the pedestal top and in the steep gradient region indicate that the dominant RMP-induced plasma transport processes are probably different in these two regions.

The changes in the T_e and n_e gradient scale lengths induced by RMPs are indicative of changes in the effective diffusivities for radial electron heat and density transport. In the edge region the effective electron thermal diffusivity is defined by [19] $\chi_e^{\text{eff}} \equiv P_{\text{cond}}(\rho)/[V'(|\nabla\rho|^2)(-n_e dT_e/d\rho)]$. Here, $V' \equiv dV/d\rho$ in which $V(\rho)$ is the volume of the ρ flux surface. Thus, to the extent that the conductive electron power flow P_{cond} and electron pressure $p_e \equiv n_e T_e$ are not changed too much by the RMPs, the ratio of the T_e gradient scale lengths with (RMP) to without (sym) RMPs is

$$\frac{[L_{T_e}]_{\text{RMP}}}{[L_{T_e}]_{\text{sym}}} \simeq \frac{\chi_e^{\text{sym}} + \chi_e^{\text{RMP}}}{\chi_e^{\text{sym}}}. \quad (1)$$

A similar relation is obtained for the ratios of the n_e gradient scale lengths. It is approximately $(D^{\text{sym}} + D^{\text{RMP}})/D^{\text{sym}}$ to the degree that the electron density n_e and radial density flow $\dot{N}(\rho)$ [19] (primarily from core fueling by energetic neutral beams at the pedestal top) is roughly constant. The edge fueling and electron density and

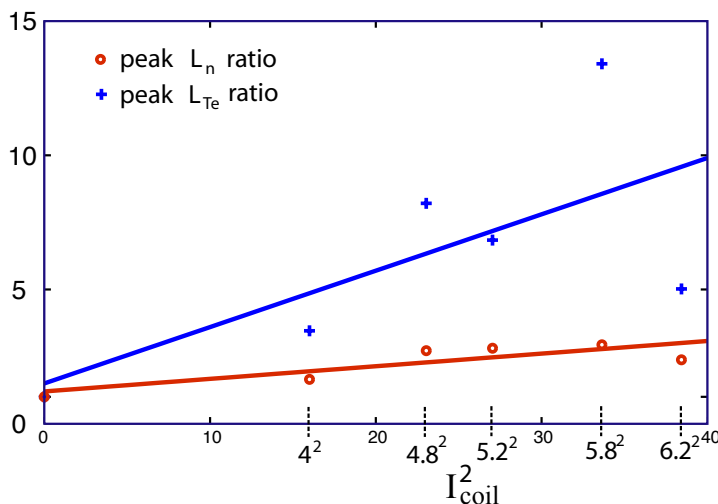


Figure 4. Peak ratios of electron temperature and density gradient scale lengths with to without RMPs increases roughly as the square of the I-coil current (kA).

pressure vary by less than a factor of about two over most of the edge region.

As shown in Fig. 3, applying RMPs increases the T_e gradient scale length by a factor $\lesssim 7$ and the n_e gradient scale length by $\lesssim 3$ at the top of the pedestal ($0.9 \lesssim \Psi_N < 0.975$). These increases indicate the effective electron thermal and density diffusivities increase by almost the same factors, i.e. $\lesssim 6$ and $\lesssim 2$. The electron thermal diffusivity profile with RMPs obtained from ONETWO interpretive transport modelling [19] (after dividing by the factor $\langle |\nabla\rho|^2 \rangle \simeq 2.17$ at $\Psi_N \simeq 0.95$) is similar to the $[L_{T_e}]_{\text{RMP}}/[L_{T_e}]_{\text{sym}}$ profile shown in Fig. 3. Also, for the two discharges in Fig. 3 the electron thermal diffusivities at $\Psi_N \simeq 0.95$ are $\chi_e^{\text{sym}} \simeq 0.6 \text{ m}^2 \text{ s}^{-1}$ and $\chi_e^{\text{sym}} + \chi_e^{\text{RMP}} \simeq 4.6 \text{ m}^2 \text{ s}^{-1}$, which indicates $\chi_e^{\text{RMP}} \simeq 4 \text{ m}^2 \text{ s}^{-1}$. This rough estimate assumes the underlying χ_e^{sym} does not change much when RMPs are applied. The experimentally-inferred $\chi_e^{\text{RMP}} \simeq 4 \text{ m}^2 \text{ s}^{-1}$ would be smaller if χ_e^{sym} was also increased by the RMPs. These values yield a ratio $(\chi_e^{\text{sym}} + \chi_e^{\text{RMP}})/\chi_e^{\text{sym}} \simeq 7.7$ in approximate agreement with the ratio of about 6.5 at $\Psi_N \simeq 0.95$ in Fig. 3. At this same flux surface the ion thermal diffusivity is smaller and does not increase as much: $(\chi_i^{\text{sym}} + \chi_i^{\text{RMP}})/\chi_i^{\text{sym}} \simeq 1.2/0.55 \simeq 2.2$.

The radial location of the rational surfaces of relevant components of the RMP fields are indicated in Fig. 3. The 5.2 kA I-coil current produces a vacuum radial magnetic perturbation $\delta B_{\rho 11/3}^{\text{vac}}$ at the $q = m/n = 11/3$ rational surface of about $6.9 \times 10^{-4} \text{ T}$. Since the toroidal field in these DIII-D ISS discharges was $B_0 \simeq 2.1 \text{ T}$, this yields $\delta B_{\rho 11/3}^{\text{vac}}/B_0 \simeq 3.3 \times 10^{-4}$. The vacuum RMPs at the other rational surfaces indicated in Fig. 3 differ by less than 15% from the magnitude of the 11/3 RMP component. Figure 3 shows that the maximum RMP-induced increases in the T_e and n_e gradient scale lengths occur just inside the 11/3 rational surface, near $\Psi_N \simeq 0.955$ for this 5.2 kA I-coil case.

The ratios of the T_e and n_e gradient scale lengths with to without RMPs increase with the I-coil current. Specifically, as shown in Fig. 4, the least square fits of the peak gradient scale length ratios increase approximately as the square of the I-coil current

(or $\delta B_{\rho m/n}^{\text{vac}}$). The larger scatter in the L_{T_e} ratio data could be due to the sensitivity of the RMP-induced effects on the T_e profiles to the q_{95} resonance conditions [12] since the location of peaks in the T_e gradient scale length ratios increase slightly with I-coil current — from $\Psi_N \simeq 0.945$ at 4 kA to $\Psi_N \simeq 0.97$ for 5.8 kA while the radial position of the $\Psi_N = 0.95$ surface varies by less than 3%. Since the slope of the peak L_{T_e} ratio is more than three times that of the peak L_n ratio, apparently $D^{\text{RMP}}/\chi_e^{\text{RMP}} \lesssim 1/3$ in the vicinity of $\Psi_N \sim 0.95$.

In the following sections pedestal plasma and tokamak device parameters will be needed to estimate various physical processes. The needed parameters will be summarized here for the 5.2 kA I-coil RMP case at the radial position $\Psi_N \simeq 0.95$, which is where Figs. 1–3 show RMPs have their largest effects on the plasma gradients. This is also the reference radial position of $q_{95} \equiv q(\Psi_N = 0.95)$. At this position the corresponding toroidal-flux-based normalized radial coordinate $\rho_N \equiv \rho/a \simeq 0.93$, in which the average radius of the separatrix in this discharge is $a \simeq 0.79$ m. For the 5.2 kA I-coil case [11, 26], at this radial position $T_e \simeq 1130$ eV, $n_e \simeq 2.5 \times 10^{19} \text{ m}^{-3}$ and $Z_{\text{eff}} \simeq 1.7$. The collisional (Braginskii [18]) parallel electron thermal diffusivity scales as $\chi_{e\parallel} \simeq v_{T_e}^2/\nu_e = \nu_e \lambda_e^2$. Here, $v_{T_e} \equiv \sqrt{2T_e/m_e}$ is the electron thermal speed, $\nu_e \simeq 5 \times 10^{-11} (n_e Z_{\text{eff}}/[T_e(\text{eV})]^{3/2}) (\ln \Lambda/17) \text{ s}^{-1}$ is the electron collision frequency and $\lambda_e \equiv v_{T_e}/\nu_e \simeq 1.2 \times 10^{-20} [T_e(\text{eV})]^2/[n_e(\text{m}^{-3}) Z_{\text{eff}} (\ln \Lambda/17)] \text{ m}$ is the electron collision length in which Z_{eff} is the effective ion charge $Z_{\text{eff}} \equiv \sum_i n_i Z_i^2/n_e$. The pedestal top parameters indicated above yield $v_{T_e} \simeq 2 \times 10^7 \text{ m s}^{-1}$, $\nu_e \simeq 5.7 \times 10^4 \text{ s}^{-1}$, $\lambda_e \simeq 350 \text{ m}$ and hence $\chi_{e\parallel} \simeq 7 \times 10^9 \text{ m}^2 \text{ s}^{-1}$. For these $n = 3$ RMP-stabilized H-mode pedestals in DIII-D the major radius is $R_0 \simeq 1.7$ m. At $\rho_N \simeq 0.93$ where $\rho \simeq 0.735$ m and $q_{95} = 3.5$, $q' \equiv dq/d\rho \simeq 12 \text{ m}^{-1}$, which yields $s \equiv \rho q'/q \simeq 2.5$ and a magnetic shear length $L_S \equiv R_0 q/s \simeq 2.4$ m. The effective poloidal wavenumber at the 11/3 surface is $k_\theta = m/\rho_{m/n} \simeq 11/0.735 \simeq 15 \text{ m}^{-1}$. The inverse magnetic field aspect ratio at this point is [19] $\epsilon \equiv (B_{\text{max}} - B_{\text{min}})/(B_{\text{max}} + B_{\text{min}}) \simeq r_M/R_0 \simeq 0.56/1.7 \simeq 0.33$. In terms of the average radial distance ρ , the distance between the $q = 10/3$ and 11/3 rational surfaces in Fig. 3 is $1/nq' \simeq 2.8$ cm. However, because of the Shafranov-shift-induced compression of the flux surfaces, the physical distance between these surfaces on the outboard midplane is about half that distance.

3. Flow screening effects on RMP-induced magnetic fields and the plasma

A working hypothesis for how RMPs stabilize ELMs is [11] that the $\delta B_{\rho m/n}$ components they induce are large enough to cause overlapping magnetic islands in the edge plasma and hence stochastisation of the magnetic field there. In a local cylindrical model the magnetic island width is $W \simeq 4\sqrt{\delta B_{r m/n} L_S/B_0 k_\theta}$ (see for example Ref. [29]) in which $k_\theta \equiv m/r$. For the 5.2 kA I-coil case being considered here, using the vacuum $\delta B_{r m/n}^{\text{vac}}/B_0 \simeq 3.3 \times 10^{-4}$ yields $W^{\text{vac}} \simeq 2.9$ cm. Since this slightly exceeds the distance between the 10/3 and 11/3 rational surfaces of $1/nq' \simeq 2.8$ cm, the Chirikov criterion [30, 31] is satisfied. Thus, this simple estimate indicates the 5.2 kA RMP-induced

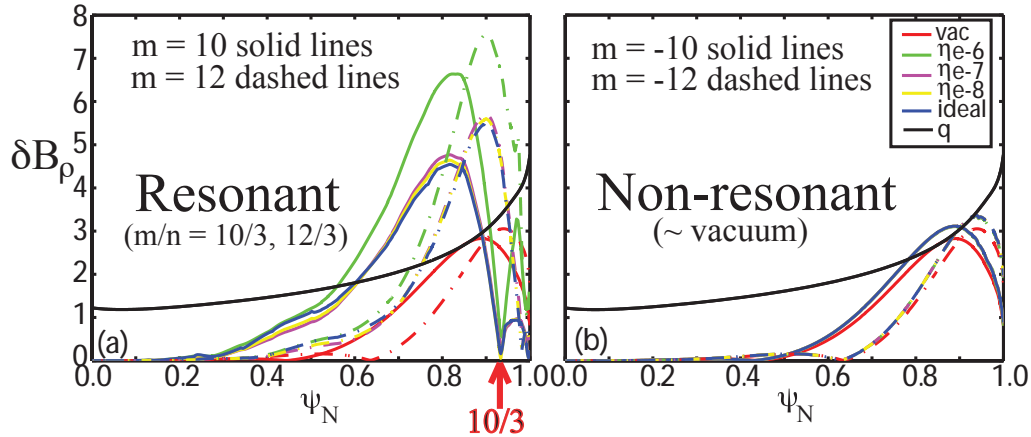


Figure 5. Normalized magnitudes of radial components of RMP-induced $\delta B_{\rho m/n}$ in a typical DIII-D H-mode plasma: (a) resonant and (b) non-resonant responses. This figure is adapted from Fig. 3 in Ref. [14]. As indicated, the 10/3 resonant component nearly vanishes at its axisymmetric rational flux surface where $q = 10/3$.

vacuum magnetic field radial perturbation strength would cause overlapping magnetic islands and hence magnetic field stochasticisation in the edge of this plasma.

However, extant toroidal plasma flow in the plasma edge can cause “flow screening” of the RMP-induced magnetic fields within the plasma [32]. If there is no flow, externally applied magnetic perturbations cause “vacuum” magnetic islands to develop at rational flux surfaces in toroidal plasmas. However, flows in the plasma can “heal” (reduce the width of) the magnetic islands [33]. If there is a very large toroidal plasma flow, the radial perturbations $\delta B_{\rho m/n}$ must vanish on their respective axisymmetric rational flux surfaces. This is usually what is obtained in ideal MHD models with toroidal flow. When dissipative effects such as plasma resistivity and viscosity are allowed for along with toroidal flows, RMP fields can “penetrate” the edge plasma, there is some reconnection of the magnetic field lines on the rational surfaces and the $\delta B_{\rho m/n}^{\text{pl}}$ is finite there. Here, the superscript pl indicates including plasma response effects.

Flow-screening effects have been simulated for DIII-D H-mode plasmas for a resistive MHD model using the MARS-F code [13, 14]; they are illustrated in Fig. 5 for (a) $m/n = 10/3, 12/3$ and (b) $m/n = -10/3, -12/3$. Figure 5(b) (right side) shows the non-resonant (i.e. $q \neq m/n$, because m is negative), reverse-helical-pitch components. They are approximately equal to the vacuum field perturbations because there are no significant plasma response effects on non-resonant field components. On the other hand, Figure 5(a) (left side) shows that the resonant components are strongly screened by the (toroidally flowing) plasma response at their rational surfaces, particularly as the plasma resistivity (the ηe label) decreases and approaches the ideal MHD state. It is useful to quantify this process by defining a factor by which the toroidal flow reduces the RMP-

induced radial magnetic perturbation at the rational flux surface where $q(r_{m/n}) \equiv m/n$:

$$f_{\text{scr}} \equiv \left[\frac{\delta B_{\rho m/n}^{\text{vac}}}{\delta B_{\rho m/n}^{\text{pl}}} \right]_{\rho_{m/n}}, \quad \text{flow screening factor.} \quad (2)$$

Estimates of this factor range from ∞ for ideal MHD, $\gtrsim 30$ for resistive MHD (for example in Fig. 5) to ~ 3 –5 if viscosity and two-fluid effects are included [15]. When significant flow screening occurs, the implied magnetic island width $W^{\text{pl}} \simeq W^{\text{vac}}/\sqrt{f_{\text{scr}}}$ becomes less than the spacing between adjacent $n = 3$ rational surfaces, the Chirikov island overlap criterion is no longer satisfied and there should be no significant magnetic field stochasticity.

A thin dissipative singular layer exists around each of the rational surfaces or magnetic island separatrices in tokamak plasmas. Magnetic reconnection of field lines takes place in this layer, which is of half-width δ (~ 0.2 cm in resistive MHD, ~ 0.5 cm [15] in the physically-relevant visco-resistive regime [34] in DIII-D pedestals).

Outside this dissipative layer the RMP-induced radial perturbation reverts to an ideal MHD response. Thus, outside this thin layer, in a cylindrical model $\delta B_{r m/n}$ should scale as r^m for $r < r_{m/n}$ and r^{-m} for $r > r_{m/n}$. Expanding these dependences in terms of the small distance away from the rational surface $x \equiv r - r_{m/n}$, this indicates that outside the layer around each rational surface (i.e. for $|x|/\delta \gg 1$) the perturbation should increase linearly as $|k_\theta x|$ in which $k_\theta \equiv m/r_{m/n}$. Far away (i.e. for $k_\theta|x| \gtrsim 1$) the magnitude of $\delta B_{r m/n}$ “saturates” and then reverts to its “global” MHD $r^{\pm m}$ behaviour — e.g. for $\Psi_N < 0.8$ and $\Psi_N > 0.97$ for the 10/3 magnetic perturbation in Fig. 5.

Taking account of both the flow screening effects near the rational surface and the linear growth away from the rational surface, the relative magnitude of the RMP-induced m/n perturbation in the plasma will be approximated as (for $|k_\theta x| \lesssim 1$)

$$\frac{\delta B_{\rho m/n}^{\text{pl}}(x)}{\delta B_{\rho m/n}^{\text{vac}}} \simeq \sqrt{1/f_{\text{scr}}^2 + k_\theta^2 x^2} \simeq \begin{cases} 1/f_{\text{scr}}, & |x| \ll 1/k_\theta f_{\text{scr}}, \\ k_\theta|x|, & |x| \gg 1/k_\theta f_{\text{scr}}. \end{cases} \quad (3)$$

The radial structure of $\delta B_{\rho m/n}^{\text{pl}}$ reproduces key aspects of the 10/3 resonant perturbation in Fig. 5a in that the perturbation is finite at the rational surface and grows approximately linearly with distance away from it in both directions. Note however that inside the 10/3 rational surface (i.e. for $\Psi_N \lesssim 0.9$) this resonant perturbation becomes even larger than the vacuum (reverse-pitch) perturbation, while outside it the perturbation amplitude saturates a short distance from the rational surface. These details of the spatial variations of the RMP-induced perturbations can be important — see section 5.

Because most of the RMP-induced $\delta B_{\rho m/n}$ components are significant throughout the edge and $k_\theta/nq' > 1$, many m/n components will likely contribute to the flutter-induced radial electron heat transport at any given radius within the pedestal top region. This can be seen by comparing the radial extent of significant 10/3 and 12/3 radial magnetic components in Fig. 5 with the spacing of rational surfaces shown in Fig. 3.

Perpendicular (radial) electron heat transport in a magnetic island region competes with parallel electron heat transport along the perturbed magnetic field in determining the electron temperature profile response. Theoretically, this effect determines a radial distance [29] $W_c^{Te} \simeq r_{m/n}(8/\epsilon sn)^{1/2}(\chi_{e\perp}/\chi_{e\parallel})^{1/4}$ over which the electron temperature structure does not follow the magnetic topology. If $W^{pl} < W_c^{Te}$ perpendicular electron heat transport dominates and the T_e profile is approximately just a function of the axisymmetric radial coordinate r or ρ . Thus, magnetic islands with $W^{pl} \lesssim W_c^{Te}$ are not theoretically predicted to produce island-type topologies in the T_e profile. Using the DIII-D pedestal parameters at $\Psi_N \simeq 0.95$ including $\chi_{e\perp} \simeq 4.6 \text{ m}^2\text{s}^{-1}$ and $\chi_{e\parallel} = \chi_{\parallel}^{\text{ref}} \simeq 1.45 \times 10^9 \text{ m}^2\text{s}^{-1}$ [see Eq. (17) in the next section] yields $W_c^{Te} \simeq 1 \text{ cm}$. Since the parallel dissipative density diffusivity effect induced by the collisional parallel ion viscosity $\eta_0^i \sim m_i n_i \chi_{i\parallel} \sim m_i n_i v_{Ti}^2 / \nu_i$ [18] is a factor of order $\sqrt{m_e/m_i} \simeq 1/60$ smaller than $\chi_{e\parallel}$ and the perpendicular density diffusivity is typically a factor of about 3 smaller than $\chi_{e\perp}$, the corresponding critical density width W_c^n is about a factor of 2.1 larger than W_c^{Te} , or about 2.1 cm for the $\Psi_N \simeq 0.95$ parameters.

The various scale lengths and their consequences for the effects due to the “thin” magnetic island topologies induced by flow-screened RMPs will now be summarized for an assumed screening factor of $f_{\text{scr}} \simeq 4$ ($\simeq 30$ for the resistive MHD model). Within the dissipative singular layer half-width $\delta \simeq 0.5$ (0.2) cm around each rational flux surface (or island separatrix) magnetic field lines are reconnecting. A magnetic island with total width $W^{pl} \simeq 1.4$ (0.5) cm would be formed at each rational surface for the assumed $f_{\text{scr}} \simeq 4$ (30). It would apparently be too thin to cause island overlap and hence magnetic stochasticity because $W^{pl} n q' \simeq 0.5$ (0.2). Also, since $W_c^{Te} \simeq 1 \text{ cm}$ ($\sim W^{pl}$) and $W_c^n \sim 2.1 \text{ cm}$ ($> W^{pl}$), the T_e and n_e profiles should not reflect the magnetic island topology very much.

Next, consider the effects of a magnetic island on the ion temperature profile. The preceding discussion focused on electron transport processes because they are the dominant transport processes along magnetic fields by a factor of $\sqrt{m_i/m_e} \sim 60 \gg 1$. Finite ion “banana widths,” collision-induced perpendicular ion heat transport and microturbulence [25] effects, all of which have scale lengths of order 1–3 cm at the pedestal top, add additional complications and tend to smear out the effects of the magnetic island structure on the T_i profile.

The net conclusion of all these theoretical considerations is that in the presence of significant flow screening effects the magnetic field induced by RMPs in the plasma mostly just non-resonantly “flutters” in space without producing strong magnetic-island-type structures in the T_e , n_e and T_i profiles. Hence, clean magnetic-island-type topologies in the T_e and n_e profiles are not likely to be experimentally observable in the DIII-D pedestals. The main cause of this smearing out of the magnetic island topology effects results from the substantial effects of perpendicular plasma transport on the relatively thin magnetic island structures around the 10/3, 11/3, 12/3 etc. rational flux surfaces. Thus, the “equilibrium” T_e and n_e profiles will be approximated to lowest order as depending only on the axisymmetric radial flux surface variable r or ρ .

4. Screw pinch model of RMP-induced flutter plasma transport

The magnetic-flutter-type radial electron transport induced by RMPs will be estimated by considering the effects of a small magnetic perturbation $\delta\mathbf{B}$ on the electrons in a “screw pinch” periodic cylinder magnetic field $\mathbf{B}_0 = B_z\hat{\mathbf{e}}_z + B_\theta\hat{\mathbf{e}}_\theta = B_z[\hat{\mathbf{e}}_z + (r/R_0q)\hat{\mathbf{e}}_\theta]$ in which $B_z \equiv B_0/(1 + r^2/R_0^2q^2)^{1/2}$ and $B_\theta = (r/R_0q)B_z$. Neglecting gyromotion, particle drifts and diamagnetic flows, which after Eq. (9) below will be shown to be negligible, electron guiding centers just stream along the magnetic field: $\mathbf{v}_g \equiv v_\parallel\mathbf{B}/B = v_\parallel(\mathbf{B}_0 + \delta\mathbf{B})/B$ where $v_\parallel \equiv \mathbf{B} \cdot \mathbf{v}_g/B$. Thus, the drift-kinetic equation (DKE) for electrons becomes

$$\frac{\partial f_e}{\partial t} + \frac{v_\parallel}{B}(\mathbf{B}_0 + \delta\mathbf{B}) \cdot \nabla f_e + \frac{d\varepsilon}{dt} \frac{\partial f_e}{\partial \varepsilon} = \mathcal{C}\{f_e\}. \quad (4)$$

Here, the total electron ($q_e = -e$) guiding center energy is $\varepsilon \equiv m_e v^2/2 - e\Phi$ in which Φ is the electrostatic potential. The lowest order equilibrium equation obtained using $d\varepsilon/dt = 0$ and neglecting $\delta\mathbf{B}$ is $(v_\parallel/B_0)\mathbf{B}_0 \cdot \nabla f_{e0} = \mathcal{C}\{f_{e0}\}$. Its solution is a Maxwellian that is constant along \mathbf{B}_0 :

$$f_{e0}(r, \varepsilon) = f_{Me} = \frac{n_e(r) e^{-e\Phi_0(r)/T_e(r)}}{[2\pi T_e(r)/m_e]^{3/2}} e^{-\varepsilon/T_e(r)}, \quad (5)$$

in which macroscopic radial (r) variations of the electron density n_e and temperature T_e , and the lowest order potential Φ_0 are indicated. Using $d\varepsilon/dt = -e[\partial\delta\Phi/\partial t + (v_\parallel/B_0)(\mathbf{B}_0 \cdot \nabla\delta\Phi)]$ plus negligible (in low β tokamak plasmas) $\delta B_\parallel \equiv \mathbf{B}_0 \cdot \delta\mathbf{B}/B_0$ and higher order terms arising from expanding $mv^2/2 = mv_\parallel^2/2 + \mu B$ using $B \equiv |\mathbf{B}| \simeq |\mathbf{B}_0 + \delta\mathbf{B}| \simeq B_0(1 + \delta B_\parallel/B_0 + \delta B^2/2B_0^2)$, the first order electron DKE for $\delta h \equiv \delta f_e - (e/T_e)\delta\Phi f_{Me}$ is

$$\frac{\partial \delta h}{\partial t} + \frac{v_\parallel}{B_0}\mathbf{B}_0 \cdot \nabla \delta h - \mathcal{C}\{\delta h\} = -\frac{v_\parallel}{B_0}\delta\mathbf{B} \cdot \nabla f_{Me}. \quad (6)$$

The non-adiabatic response δh is induced by the spatial magnetic flutter [16] $\delta B_r(\mathbf{x}, t) \equiv \hat{\mathbf{e}}_r \cdot \delta\mathbf{B}$ of field lines radially across the plasma profile gradients:

$$\begin{aligned} \delta\mathbf{B} \cdot \nabla f_{Me} &= \delta B_r [\partial f_{Me}/\partial r] \varepsilon \\ &= \delta B_r f_{Me} \left[\frac{d \ln p_e}{dr} - \frac{e}{T_e} \frac{d\Phi_0}{dr} + \left(\frac{m_e v^2}{2T_e} - \frac{5}{2} \right) \frac{d \ln T_e}{dr} \right]. \end{aligned} \quad (7)$$

For simplicity, a Krook model will be used for the collision operator: $\mathcal{C}\{\delta h\} \simeq -\nu_{\text{eff}}\delta h$ in which ν_{eff} is an effective electron collision frequency. At the top of H-mode pedestals the electron collision length λ_e is usually long compared to the poloidal periodicity length: $\lambda_e/(2\pi R_0q) \sim 350/37 \sim 10$ for the DIII-D pedestal top at $\Psi_N \simeq 0.95$. Trapped electrons do not carry any parallel (to \mathbf{B}_0) flow over the relevant distances (up to $\sim \lambda_e$). Rather, only untrapped (or circulating) electrons carry the density flows and heat fluxes over these long parallel distances. For a lowest order Maxwellian distribution, the fraction of trapped particles is $n_t/n_0 = \sqrt{1 - B(\theta)/B_{\text{max}}}$, which varies with the poloidal angle θ . For simplicity, it will be assumed that $B(\theta) \simeq B_0(1 - \epsilon \cos \theta)$. When averaged over a magnetic flux surface, the average fraction of trapped particles is $\langle n_t \rangle/n_0 =$

$(2/\pi)\sqrt{\Delta B/B_{\max}} + \mathcal{O}\{\epsilon^2\}$ in which $B_{\max} \simeq B_0(1 + \epsilon)$ and $\Delta B \equiv B_{\max} - B_{\min} \simeq 2\epsilon B_0$. Thus, the average fraction of untrapped particles is $\langle n_{ut} \rangle / n_0 \simeq 1 - (2/\pi)\sqrt{\Delta B/B_{\max}}$, which is about 0.55 for $\epsilon \simeq 0.33$. Hence, an approximate effective electron collision frequency for untrapped electrons is $\nu_{\text{eff}} \sim \nu_e / (\langle n_{ut} \rangle / n_0)^2$, which is $\sim 3.3\nu_e \sim 2 \times 10^5 \text{ s}^{-1}$ for DIII-D pedestal parameters at $\Psi_N \simeq 0.95$.

The non-adiabatic response δh induced by a single m/n magnetic field component induced by the externally applied RMP will be determined first. The radial component of a resonant m, n magnetic perturbation will be represented by:

$$\begin{aligned} \delta B_{r m/n}(\mathbf{x}, t) &= \delta \hat{B}_{r m/n}(r) \cos(m\theta - nz/R_0 - \omega t + \varphi_{mn}) \\ &= \delta \hat{B}_{r m/n}(r) \mathcal{R}e \left\{ e^{i(m\theta - nz/R_0 - \omega t + \varphi_{mn})} \right\}. \end{aligned} \quad (8)$$

Here, the Fourier coefficient $\delta \hat{B}_{r m/n}$ is real, φ_{mn} is an arbitrary phase factor and ω represents a possible sinusoidal time-dependence.

For the screw pinch magnetic field model $\mathbf{B}_0 \cdot \nabla \delta h = B_z [\partial/\partial z + (1/R_0 q)(\partial/\partial \theta)] \delta h$. Thus, using the representation of $\delta B_{r m/n}$ in (8), the first order partial differential equation in (6) can be written in terms of its mathematical characteristic curves [electron trajectories: $r' = r$, $\theta' = \theta + (z' - z)/R_0 q$, $z' = z + v_{\parallel}(t' - t)(B_z/B_0)$, $v'_{\parallel} = v_{\parallel}$] as $e^{-\nu_{\text{eff}} t'} (d/dt') [e^{\nu_{\text{eff}} t'} \delta h(t')] = \left[(v_{\parallel}/B_0) \delta B_{r m/n} (df_{Me}/dr) \right]_{\mathbf{x}', t'}$, which can be integrated to yield for the $\cos(m\theta - nz/R_0 - \omega t + \varphi_{mn})$ part δh^c of the response δh :

$$\begin{aligned} \delta h^c(t) &= \delta h^c(t'=0) e^{-\nu_{\text{eff}} t} - \int_0^t dt' e^{\nu_{\text{eff}}(t'-t)} \frac{v'_{\parallel}}{B_0} \mathcal{R}e \left\{ \delta B_{r m/n}(\mathbf{x}', t') \right\} \frac{\partial f_{Me}}{\partial r} \\ &= -v_{\parallel} \frac{\delta B_{r m/n}(\mathbf{x}, t)}{B_0} \frac{\partial f_{Me}}{\partial r} \mathcal{R}e \int_0^t dt' e^{i[k_{\parallel}(x)v_{\parallel} - (\omega + i\nu_{\text{eff}})](t'-t)} \\ &= -v_{\parallel} \frac{\delta B_{r m/n}(\mathbf{x}, t)}{B_0} \frac{\partial f_{Me}}{\partial r} \left\{ \frac{\nu_{\text{eff}}}{[k_{\parallel}(x)v_{\parallel} - \omega]^2 + \nu_{\text{eff}}^2} \right\}. \end{aligned} \quad (9)$$

The initial condition is neglected on the last line because the ‘‘equilibrium’’ response for $t \gg 1/\nu_{\text{eff}}$ ($\sim 0.5 \mu\text{s}$) is desired.

In (9) $k_{\parallel}(x) \equiv (B_z/B_0)(m - nq)/R_0 q$ is the effective parallel wavenumber in the sheared magnetic field. Close to a rational flux surface it simplifies to $k_{\parallel}(x) \simeq k'_{\parallel} x$ with $k'_{\parallel} \simeq -nq'/R_0 q = -k_{\theta}/L_S$ for standard large aspect ratio tokamak ordering with $r/R_0 q \ll 1$ so $B_z \simeq B_0$ and $q \simeq q(r_{m/n}) + xq'$ in which $r_{m/n}$ is the rational surface where $q(r_{m/n}) = m/n$, $x \equiv r - r_{m/n}$ and $q' \equiv dq/dr|_{r_{m/n}}$ represents the magnetic shear.

The real frequency ω represents a combination of the Doppler frequency induced by poloidal and toroidal plasma flows relative to the laboratory rest frame, and any oscillation frequency in the I-coil current that imposes the RMPs. For example, the plasma toroidal rotation frequency at $\Psi_N \simeq 0.95$ is $\Omega_t \simeq 8 \times 10^3 \text{ rad s}^{-1}$. Typical diamagnetic flow, curvature and grad- B electron drift frequencies are of the same order: $\omega_{*e} = k_{\theta}(T_e/eB_0 L_n) \sim 4 \times 10^4 \text{ rad s}^{-1}$ and $\omega_{de} \sim k_{\theta}(2T_e/eB_0 R_0) \sim 10^4 \text{ rad s}^{-1}$ at the top of RMP-suppressed H-mode pedestals in DIII-D. Thus, all these frequencies are about an order of magnitude smaller than the effective electron collision damping rate

ν_{eff} ($\gtrsim 2 \times 10^5 \text{ s}^{-1}$ for the DIII-D $\Psi_n \simeq 0.95$ parameters). Hence, possible effects of ω , ω_{*e} and ω_{de} will all be neglected.

The δh^c in (9) is odd in v_{\parallel} . Thus, $\int d^3v \delta h^c = 0$ yields the adiabatic electron response $\delta n_e^c = n_e(e/T_e)\delta\Phi$. A similar ion analysis yields the adiabatic ion response $\delta n_i^c = -n_i(Z_i e/T_i)\delta\Phi$. The perturbed quineutrality condition $\delta n_e^c = Z_i \delta n_i^c$ requires $\delta\Phi = 0$. Thus, there is no RMP-induced electron density response and $\delta f_e^c = \delta h^c$.

In the screw pinch model the parallel (to \mathbf{B}_0) electron flow $\delta V_{e\parallel}^c$ and heat flux $\delta q_{e\parallel}^c$ induced by the magnetic flutter component $\delta B_{r\,m/n}$ are thus

$$\begin{aligned} \begin{bmatrix} n_e \delta V_{e\parallel}^c \\ \delta q_{e\parallel}^c \end{bmatrix} &\equiv \int_{ut} d^3v v_{\parallel} \begin{bmatrix} L_0^{3/2} \\ T_e L_1^{3/2} \end{bmatrix} \delta f_e^c \\ &= -n_e \frac{\delta B_{r\,m/n}}{B_0} \begin{bmatrix} D_{e\parallel}^{\text{eff}} d \ln \hat{p}_e / dr \\ \chi_{e\parallel}^{\text{eff}} dT_e / dr \end{bmatrix}. \end{aligned} \quad (10)$$

Here, $L_0^{3/2} \equiv 1$ and $L_1^{3/2} \equiv (m_e v^2 / T_e - 5/2)$ are Laguerre polynomial functions of the normalized electron kinetic energy $m_e v^2 / 2T_e$. The relevant thermodynamic forces here are $d \ln \hat{p}_e / dr \equiv d \ln p_e / dr - (e/T_e)(d\Phi_0/dr)$ and dT_e/dr . Note that only the $\cos(m\theta - nz/R_0 - \omega t + \varphi_{mn})$ components of δh and the density flow and heat flux have been determined here. They all represent sinusoidal effects that are in phase with the helical pitch of the resonant field lines where $q(r_{m/n}) = m/n$.

A Padé-approximate [35] effective parallel electron thermal diffusivity is (for ν_{eff} independent of the electron speed v)

$$\begin{aligned} \chi_{e\parallel}^{\text{eff}} &\simeq \frac{v_{Te}^2}{\nu_{\text{eff}}} \frac{c_{\nu T} \nu_{\text{eff}}^2}{\nu_{\text{eff}}^2 + k_{\parallel}^2 v_{Te}^2 / c_{\parallel}^2} = c_{\nu T} \frac{v_{Te}^2}{\nu_{\text{eff}}} \frac{1}{1 + x^2 / \delta_{\parallel}^2} \\ &\simeq \begin{cases} \frac{c_{\nu T} v_{Te}^2}{\nu_{\text{eff}}}, & |x| \equiv |r - r_{m/n}| \ll \delta_{\parallel}, \\ \frac{c_{\nu T} c_{\parallel}^2 \nu_{\text{eff}}}{k_{\parallel}^2}, & |x| \equiv |r - r_{m/n}| \gg \delta_{\parallel}. \end{cases} \end{aligned} \quad (11)$$

Electron collisions embodied in ν_{eff} provide the irreversibility that causes the finite parallel electron flows. Here, δ_{\parallel} is the characteristic radial layer width which is defined in (13) below. The parallel density diffusivity $D_{e\parallel}^{\text{eff}}$ has the same form but with coefficient $c_{\nu n}$. The magnetic shear causes $\chi_{e\parallel}^{\text{eff}}$ and $D_{e\parallel}^{\text{eff}}$ in (11) to decrease as $1/x^2$ for $|x| \gg \delta_{\parallel}$.

For a ν_{eff} independent of v , the various coefficients are

$$c_{\nu T} = \frac{5}{4} \frac{\langle n_{ut} \rangle}{n_0}, \quad c_{\nu n} = \frac{1}{2} \frac{\langle n_{ut} \rangle}{n_0}, \quad c_{\parallel} = \sqrt{2}, \quad (12)$$

in which the $\langle n_{ut} \rangle / n_0$ accounts for the fact that only untrapped particles contribute to these parallel flows. The $\chi_{e\parallel}^{\text{eff}}$ is larger than the density diffusivity $D_{e\parallel}^{\text{eff}}$ by a factor of $c_{\nu T} / c_{\nu n} = 5/2$ for a constant ν_{eff} and even larger for a Lorentz-model collision frequency $\nu_{\text{eff}} \propto 1/v^3$. If ν_{eff} is taken to be the electron collision frequency ν_e and $\langle n_{ut} \rangle / n_0$ is set to unity, for $|x| \ll \delta_{\parallel}$ this parallel electron thermal diffusivity factor of $5/4$ is close to the Braginskii [18] collisional parallel electron thermal diffusivity for which $c_{\nu T} = 1.6$.

Since $k_{\parallel}(x) \simeq k'_{\parallel}x$, the parameter that characterizes the radial extent over which magnetic flutter induces the largest parallel electron heat flux and density flow is

$$\delta_{\parallel} \equiv \frac{c_{\parallel} \nu_{\text{eff}}}{|k'_{\parallel}| v_{Te}} = c_{\parallel} \frac{L_S}{k_{\theta} \lambda_e} \left(\frac{n_0}{\langle n_{ut} \rangle} \right)^2, \quad (13)$$

in which $\nu_{\text{eff}} \simeq \nu_e / \langle n_{ut} / n_0 \rangle^2 \simeq 3.3 \nu_e$ has been used to take account of the fact that only the fraction $\langle n_{ut} / n_0 \rangle \simeq 0.55$ of untrapped electrons carry these parallel flows. For the DIII-D pedestal parameters $\delta_{\parallel} \simeq 0.22$ cm. Since the parallel electron flow implies a parallel current $-n_e e \delta V_{e\parallel}$, this is also roughly the total radial width $2\delta_{\eta}$ over which magnetic field lines are being reconnected in the resistive MHD model, i.e. $\delta_{\parallel} \sim \delta_{\eta}$.

The parallel electron flow induces a radial electron density flux that is generated by the electron guiding center motion along a magnetic field \mathbf{B} which has an in-phase spatially fluttering radial magnetic field component δB_r : $\Gamma_e^{\delta B} \equiv \langle \hat{\mathbf{e}}_r \cdot \int d^3v \mathbf{v}_g f_e \rangle = \int d^3v \langle (v_{\parallel} \hat{\mathbf{e}}_r \cdot \delta \mathbf{B} / B_0) \delta f_e^c \rangle = \langle n_e \delta V_{e\parallel}^c \delta B_r / B_0 \rangle$. Here, $\langle \dots \rangle$ indicates the flux surface average, which for the cylindrical screw-pinch model is $\langle f \rangle \equiv [1/(2\pi)^2] \int_0^{2\pi} dz/R_0 \int_0^{2\pi} d\theta f(z, \theta)$. A nonzero average density flux is induced by the component of $\delta V_{e\parallel}^c$ that is in phase with the RMP-induced $\delta B_{r\,m/n}$: $\Gamma_e^{m/n} = n_e \delta \hat{V}_{\parallel m/n}^c \delta \hat{B}_{r\,m/n} / 2B_0$. A parallel electron heat flux similarly induces a radial electron heat flux. Thus, the magnetic-flutter-induced radial electron density and heat fluxes are

$$\begin{aligned} \begin{bmatrix} \Gamma_e^{m/n} \\ \Upsilon_e^{m/n} \end{bmatrix} &\equiv \begin{bmatrix} n_e V_{er} \\ q_{er} \end{bmatrix} = \begin{bmatrix} \langle n_e \delta \hat{V}_{e\parallel}^c \delta \hat{B}_{r\,mn}^{\text{pl}} \rangle \\ \langle \delta \hat{q}_{e\parallel}^c \delta \hat{B}_{r\,mn}^{\text{pl}} \rangle \end{bmatrix} \\ &= -n_e \begin{bmatrix} D_e^{m/n} d \ln \hat{p}_e / dr \\ \chi_e^{m/n} dT_e / dr \end{bmatrix}. \end{aligned} \quad (14)$$

The detailed specification of $\chi_e^{m/n}(x)$ and $D_e^{m/n}(x)$ is complicated by the fact that both of its key factors, $\chi_e^{\text{eff}}(x)$ from the combination of (10) and (11) and $\delta \hat{B}_{r\,m/n}^{\text{pl}}(x)$ from (3), vary rapidly with the distance $x \equiv r - r_{m/n}$ off the rational surface at $r_{m/n}$. And their dependences cancel at large $|x|$. Also, the radial extent $1/k_{\theta}$ (~ 6.7 cm in DIII-D pedestals) of the spatially linearly growing RMP-induced components $\delta \hat{B}_{r\,m/n}$ is usually larger than the spacing between rational surfaces $1/nq'$ ($\simeq 2.8$ cm). Thus, typically the $\chi_e^{m/n}$ diffusivities from a number of m/n rational surfaces will overlap to produce the total RMP-induced electron heat diffusivity at a given plasma radius. Hence, the radii at which the various quantities are to be evaluated needs to be specified carefully.

In what follows the cylindrical screw pinch model minor radius r is adapted to the tokamak magnetic geometry by taking it to be the toroidal-flux-based average minor radius ρ . Substituting the approximate assumed form for $\delta B_{\rho\,m/n}^{\text{pl}}$ from (3) and the result for χ_e^{eff} from (11) into (14) yields a result that can be written as

$$\chi_e^{m/n} = \chi_{m/n}^{\text{ref}}(\rho) F_{m/n}(x). \quad (15)$$

Here, at plasma radius ρ the reference radial electron thermal diffusivity induced by each m/n component of the RMP-induced field is in general

$$\chi_{m/n}^{\text{ref}}(\rho) \equiv \frac{1}{2} \left[\frac{\delta \hat{B}_{\rho\,m/n}^{\text{vac}}(\rho_{m/n})}{B_0} \right]^2 \chi_{\parallel}^{\text{ref}}(\rho) [k_{\theta} \delta_{\parallel}]_{\rho_{m/n}}^2. \quad (16)$$

The reference parallel electron thermal diffusivity is

$$\chi_{\parallel}^{\text{ref}}(\rho) \equiv c_{\nu T} \frac{v_{Te}^2}{\nu_{\text{eff}}} \simeq \frac{5}{4} \left[\frac{\langle n_{ut} \rangle}{n_0} \right]^3 \frac{v_{Te}^2}{\nu_e}. \quad (17)$$

The analogous magnetic-flutter-induced radial density diffusivity $D_e^{m/n}$ has the same form but with $\chi_{e\parallel}^{\text{eff}} \rightarrow D_{e\parallel}^{\text{eff}}$ and hence $c_{\nu T} \rightarrow c_{\nu n}$, i.e. $5/4 \rightarrow 1/2$ for a constant ν_{eff} . For the DIII-D pedestal parameters at $\Psi_N \simeq 0.95$, $\chi_{\parallel}^{\text{ref}} \simeq 1.45 \times 10^9 \text{ m}^2 \text{ s}^{-1}$. At $\rho_{m/n}$ the key factor in (16) can be written as $\chi_{\parallel}^{\text{ref}}(k_{\theta}\delta_{\parallel})^2 = (5n_0/2\langle n_{ut} \rangle)\nu_e L_S^2$.

The dimensionless factor that accounts for spatial variations of both the plasma-screening of the RMP-induced fields and $\chi_{e\parallel}^{\text{eff}}$ for this cylindrical screw pinch model adapted to the tokamak geometry is

$$\begin{aligned} F_{m/n}(x) &\equiv \frac{1}{[k_{\theta}\delta_{\parallel}]_{\rho_{m/n}}^2} \left[\frac{\delta \hat{B}_{\rho_{m/n}}^{\text{pl}}(x)}{\delta \hat{B}_{\rho_{m/n}}^{\text{vac}}(\rho_{m/n})} \right]^2 \frac{\chi_{e\parallel}^{\text{eff}}(x)}{\chi_{\parallel}^{\text{ref}}(\rho_{m/n})} \\ &\simeq \frac{C_{\text{scr}}^2 + X^2}{1 + X^2}. \end{aligned} \quad (18)$$

In this equation's second line the normalized distance from the m/n rational surface is

$$X \equiv \frac{x}{[\delta_{\parallel}]_{\rho_{m/n}}} \equiv \frac{\rho - \rho_{m/n}}{[\delta_{\parallel}]_{\rho_{m/n}}} \quad (19)$$

and the key dimensionless screening factor parameter is

$$C_{\text{scr}} = 1/(f_{\text{scr}}[k_{\theta}\delta_{\parallel}]_{\rho_{m/n}}). \quad (20)$$

The first line of (18) gives the general definition of $F_{m/n}$. The approximate form on its second line uses (3); it is only valid for $|x| \lesssim 1/k_{\theta}$ or $|X| \lesssim 1/(k_{\theta}\delta_{\parallel})$, which is ~ 30 for DIII-D pedestals, since the global MHD responses saturate and no longer increase linearly with X beyond about this distance from the rational surface.

Near the 11/3 resonance the parameter C_{scr} in (18) is about unity for $f_{\text{scr}} \simeq 30$ but about 7.6 for $f_{\text{scr}} \simeq 4$ for the DIII-D pedestal parameters at $\Psi_N \simeq 0.95$. Thus, this parameter is usually $\gtrsim 1$. Hence, the function $F_{m/n}(X)$ has the following properties: 1) for $|X|^2 \ll 1$, $F_{m/n} \simeq C_{\text{scr}}^2$; 2) for $1 \ll |X|^2 \ll C_{\text{scr}}^2$, $F_{m/n} \simeq C_{\text{scr}}^2/X^2$ and 3) for $|X|^2 \gg C_{\text{scr}}^2$, $F_{m/n} \rightarrow 1$. Since in the $f_{\text{scr}} = 30$ case, $C_{\text{scr}} \simeq 1$ and hence $F_{m/n}$ is spatially approximately constant. In contrast, in the $f_{\text{scr}} = 4$ case $F_{m/n}$ varies from $C_{\text{scr}}^2 \sim 60$ on the rational surface to unity far away, which implies that χ_e^{mn} is very large near the rational surface but decreases rapidly away from it and ultimately becomes constant.

The total RMP-induced radial electron density and thermal diffusivities are obtained by summing over all the relevant m, n magnetic field components:

$$D_e^{\text{RMP}} \equiv \sum_n \sum_m D_e^{m/n} \rightarrow \sum_m D_e^{m/3}, \quad (21)$$

$$\chi_e^{\text{RMP}} \equiv \sum_n \sum_m \chi_e^{m/n} \rightarrow \sum_m \chi_e^{m/3}. \quad (22)$$

As indicated in the last forms, since the $n = 3$ components will be assumed to be dominant for the RMPs applied to the DIII-D pedestals [11], the sum is simplified to

just the $m/3$ components. However, the magnetic-flutter-induced electron transport effects of the $n = 1, 2$ error and C-coil fields should in general be added in here as well.

In situations where the radial electron thermal diffusivity χ_e varies significantly with radius, the average radial transport flux and hence maximum T_e gradient is dominated by regions where χ_e is smallest [36]. To demonstrate this simply, note that in the pedestal region there is little local heating. Hence electron heat mainly just flows radially through it [19]. Thus, the local electron temperature gradient in the pedestal region is determined by the radial heat flow P_{cond} divided by the radial conductive electron heat flow speed $V'\langle|\nabla\rho|^2\rangle n_e\chi_e$ at that radius [19]:

$$-\frac{dT_e}{d\rho} \simeq \frac{P_{\text{cond}}}{V'\langle|\nabla\rho|^2\rangle n_e\chi_e}. \quad (23)$$

The T_e gradient will be largest where $n_e\chi_e$ is smallest. Hence, from (22) and (15), the relevant function for assessing the effect of the spatially varying $\chi_e^{\text{RMP}}(\rho)$ on the electron temperature gradient profile and average radial transport is $1/\sum_{mn} F_{m/n}(x)$.

The effective RMP-induced radial electron thermal diffusivity in the DIII-D edge will now be estimated in the region between the 10/3 and 11/3 surfaces for the resistive MHD $f_{\text{scr}} \simeq 30$ and visco-resistive $f_{\text{scr}} \simeq 4$ cases. Since the distance $1/k_\theta \simeq 6.7$ cm is 2.4 times the distance $1/nq' \simeq 2.8$ cm between rational surfaces, there are about 6 relevant RMP components to consider: 8/3, 9/3, 10/3, 11/3, 12/3 and 13/3. For a simplest possible estimate it will be assumed that these components: 1) have equal vacuum amplitudes $\delta\hat{B}_{r/m/n}^{\text{vac}}/B_0 \simeq 3.3 \times 10^{-4}$ on their respective rational surfaces, 2) have the same δ_{\parallel} ($\simeq 0.22$ cm) thermal diffusivity layer widths on their rational surfaces, 3) are equally spaced in the edge region and 4) the electron density n_e does not vary significantly between the 10/3 and 11/3 rational surfaces. With these assumptions, (16) yields $\chi_{11/3}^{\text{ref}} \simeq (1/2)(3.3 \times 10^{-4})^2(1.45 \times 10^9) [(15)(0.0022)]^2 \simeq 0.086 \text{ m}^2 \text{ s}^{-1}$.

In the resistive MHD case in which $f_{\text{scr}} \simeq 30$ one obtains $C_{\text{scr}} \simeq 1$. Since this yields a spatially constant $F_{m/n} \simeq 1$, the sum over the 6 relevant components in this case just yields 6. Hence, (22) yields $\chi_e^{\text{RMP}} \simeq \sum_m \chi_e^{m/3} \simeq 6 \chi_{11/3}^{\text{ref}} \simeq 0.5 \text{ m}^2 \text{ s}^{-1}$ for the strong flow screening of the resistive MHD model [14].

Figure 6 shows a plot of the inverse of the relevant $F_{m/3}$ factors and the inverse of their sum between the 10/3 and 11/3 rational surfaces for the $f_{\text{scr}} = 4$ screening factor case. Since this case has $C_{\text{scr}} \simeq 7.6$, the $F_{10/3}$ and $F_{11/3}$ factors vary a lot between these rational surfaces. In this simplified model the maximum in the inverse of the sum of the 6 relevant factors occurs half way between adjacent rational surfaces. Hence, the maximum electron temperature gradient also occur there and the minimum gradients occur at the rational surfaces, as illustrated in Fig. 7.

The predicted T_e profiles in Fig. 7 have been obtained by integrating Eq. (23) inward from the $\rho_{11/3}$ rational surface assuming for illustrative purposes that $T_e(\rho_{11/3}) \simeq 1$ keV. For the $f_{\text{scr}} = 30$ resistive MHD flow-screening model [14] the constant electron temperature gradient here is $dT_e/d\rho \simeq (1/6) \text{ keV}/[\rho_{10/3} - \rho_{11/3}]$, which yields $\chi_e^{\text{RMP}} \simeq 6 \chi_{11/3}^{\text{ref}} \simeq 0.5 \text{ m}^2 \text{ s}^{-1}$, as indicated previously. If one assumes the effective electron thermal diffusivity is determined by the radial transport at the mid-point

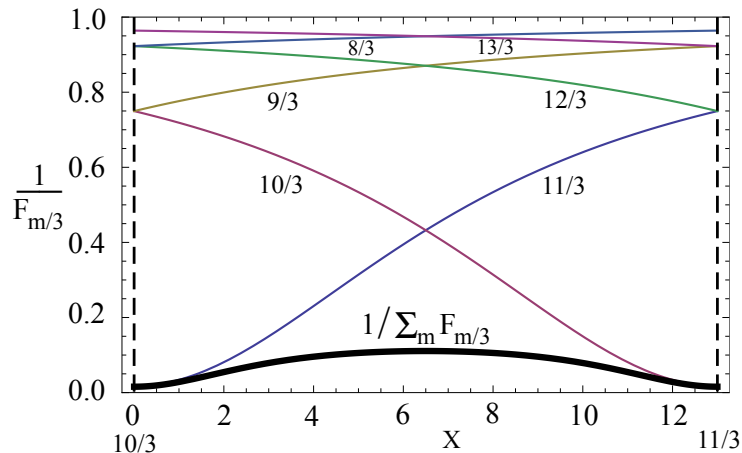


Figure 6. Inverse of the $F_{m/3}(X)$ functions for $m = 8, 9, 10, 11, 12, 13$ between the $10/3$ ($X = 0$) and $11/3$ ($X = 13$) rational surfaces in the visco-resistive case with $f_{\text{scr}} = 4$. The dark solid line shows the inverse of the sum of these contributions.

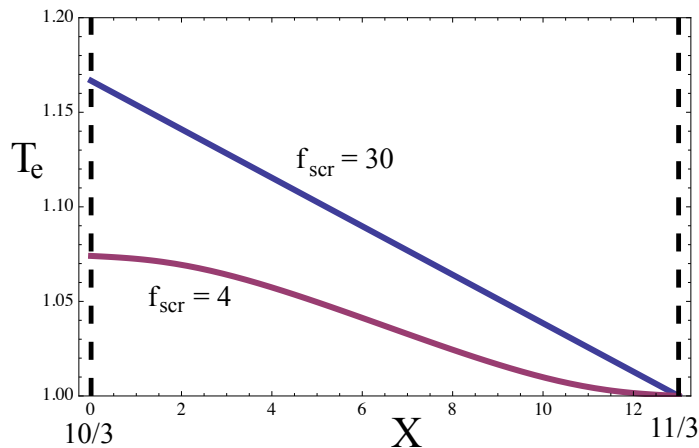


Figure 7. Schematic illustration of the predicted electron temperature (keV) profile in the $\sim 1/nq' \simeq 2.8$ cm between the $10/3$ and $11/3$ rational surfaces for the $f_{\text{scr}} = 30$ (resistive MHD model [14]) and the $f_{\text{scr}} = 4$ visco-resistive MHD model [15].

between adjacent rational surfaces where $1/\sum_m F_{m/3} \simeq 0.11$, the estimated RMP-induced radial electron thermal diffusivity is $\chi_e^{\text{RMP}} \simeq (1/0.11) \chi_{11/3}^{\text{ref}} \simeq 0.8 \text{ m}^2 \text{ s}^{-1}$ for the visco-resistive [15] weak shielding case. More precisely, an average electron temperature gradient between the $10/3$ and $11/3$ surfaces can be defined by $\Delta T_e / \Delta \rho \equiv [T_e(\rho_{10/3}) - T_e(\rho_{11/3})] / [\rho_{10/3} - \rho_{11/3}] \simeq -0.074 \text{ keV} / \Delta \rho$. This yields an average RMP-flutter-induced electron thermal diffusivity of $\bar{\chi}_e^{\text{RMP}} \simeq 1.2 \text{ m}^2 \text{ s}^{-1}$ for the $f_{\text{scr}} = 4$ visco-resistive MHD flow-screening model [15]. If a substantial magnetic island with $W^{\text{pl}} > W_c^{\text{Te}}$ was present on either of the rational surfaces highlighted in Fig. 7, the T_e profile would be flattened [37] up to a distance of $W^{\text{pl}}/2$ away from the rational surface, and the predicted average $\bar{\chi}_e^{\text{RMP}}$ would be increased somewhat further.

5. Comparisons of flutter transport theory to experimental data

The predictions of the flutter-based model of radial electron transport in the preceding section will now be compared both qualitatively and quantitatively with the RMP effects data discussed in section 2. Two generic predictions of the model agree with the DIII-D data. First, the increases of the T_e and n_e gradient scale lengths induced by the RMPs scaling approximately with I_{coil}^2 as shown in Fig. 3 agrees with the scaling of χ_e^{RMP} and D_e^{RMP} with $[\delta B_{\rho m/n}^{\text{vac}}]^2$. Second, the larger increase of T_e gradient scale lengths compared to those for n_e and the consequent experimental inference that $D_e^{\text{RMP}}/\chi_e^{\text{RMP}} \lesssim 1/3$ in the pedestal top region agrees with the flutter model prediction that $D_e^{\text{RMP}}/\chi_e^{\text{RMP}} \leq 2/5$. In contrast, the Rechester-Rosenbluth stochastic magnetic field model [17] predicts $D_e^{\text{stoch}}/\chi_e^{\text{stoch}} \sim \sqrt{m_e/m_D} \sim 1/60$ and disagrees with these experimental results.

In addition, the peaking of the T_e and n_e gradient scale length ratios at $\Psi_N \simeq 0.955$ shown in Fig. 3 agrees qualitatively with the model's predictions: a strong decrease of $\chi_e^{\text{RMP}} \propto \chi_{\parallel}^{\text{ref}}(\rho) \propto T_e^{5/2}/n_e Z_{\text{eff}}$ and decreased magnitudes of the $\delta \hat{B}_{\rho m/n}$ in the pedestal's steep gradient region ($\Psi_N \gtrsim 0.97$), and generic r^m decreases of the $m/3$ RMP-induced magnetic components for $\Psi_N < 0.9$. However, these arguments alone probably do not explain the experimentally observed narrow $q_{95} \sim 3.5$ resonance window for RMP stabilisation of ELMs in the DIII-D ISS discharges [11, 12].

Also, since the RMP-induced flutter electron transport becomes negligible in the lower T_e region of the steep gradient region of the pedestal, other processes probably govern the qualitatively different electron transport there — perhaps non-ambipolar electron density transport [26, 38] induced by open-field-lines (because extended MHD dissipative layer widths exceed the rational surface spacing there?) plus dominant paleoclassical radial electron heat transport [39] there.

Finally, the modest RMP-induced increase in the ion thermal diffusivity χ_i , which could be due mainly to changes in the anomalous plasma transport caused by RMP-induced reductions in the T_e and n_e gradients, is much smaller than the electron χ_e increases in the 5.2 kA I-coil case. This agrees qualitatively with the much smaller parallel and consequently radial transport processes by ions than electrons in the flutter transport model where $\chi_i^{\text{RMP}}/\chi_e^{\text{RMP}} \sim \chi_{i\parallel}/\chi_{e\parallel} \sim \sqrt{m_e/m_D} \sim 1/60 \ll 1$.

While the simplest possible RMP-flutter-induced electron thermal diffusivity estimates obtained here are comparable to or larger than the effective diffusivities in the absence of RMPs ($\chi_e^{\text{sym}} \simeq 0.6 \text{ m}^2 \text{ s}^{-1}$), quantitatively these predictions are somewhat smaller than the experimentally inferred values with RMPs. Namely, at $\Psi_N \simeq 0.95$ the flutter model predictions of $\chi_e^{\text{RMP}} \simeq 0.5 \text{ m}^2 \text{ s}^{-1}$ (strong flow screening, $f_{\text{scr}} \simeq 30$) and $\bar{\chi}_e^{\text{RMP}} \simeq 1.2 \text{ m}^2 \text{ s}^{-1}$ (weak flow screening, $f_{\text{scr}} \simeq 4$) are a factor of 3–8 smaller than the experimentally-inferred maximum $\chi_e^{\text{RMP}} \simeq 4 \text{ m}^2 \text{ s}^{-1}$ induced by the RMPs for an I-coil current of 5.2 kA. The model predictions could become larger if: 1) extended MHD modeling predictions for $\delta \hat{B}_{r m/n}^{\text{pl}}(x)$ were used in evaluating χ_e^{RMP} from a combination of the general forms in (22), (15) and (18), 2) there was less flow screening on the 10/3 or 11/3 rational surfaces, or 3) the plasma response physics was different for some of the

m/3 components and this caused a different radial structure and larger magnitude of the RMP-induced $\delta\hat{B}_{r_{m/3}}^{\text{pl}}(x)$ profiles near $\Psi_N = 0.95$. The last two possibilities could provide interpretations for the narrow $q_{95} \sim 3.5$ resonance window observed for ELM stabilisation [11] if the plasma response to the RMP 10/3, 11/3 and/or 12/3 components were larger in the vicinity of $\Psi_N = 0.95$ than the analytic response function in (3) that was used in making the estimates of $\bar{\chi}_e^{\text{RMP}}$ in this paper.

The effects of the tokamak magnetic field geometry are important for precise quantitative predictions. A theoretical model of them is currently being developed [40]. Since the electron collision length $\lambda_e \simeq 350$ m is very long compared to the poloidal periodicity length along field lines of $2\pi R_0 q \simeq 37$ m, the electron responses to RMP fields should be averaged over the magnetic flux surface. Also, since $|\mathbf{B}_0(\theta)|$ varies significantly over a flux surface (factor ~ 2 for the DIII-D pedestals), so does the $v_{\parallel}(\theta)$ of circulating (“untrapped”) electrons in the RMP-drive term in the flutter drift-kinetic equation (6). Further, this DKE should be solved with a more precise Lorentz Coulomb collision operator rather than with the adapted Krook model being used here. Finally, because of the large inverse aspect ratio ϵ (~ 0.33 for DIII-D pedestals) and the nearness of the pedestal region to the magnetic separatrix, the details of the tokamak magnetic field geometry are important both in the representation of RMP-induced magnetic perturbations in the plasma including finite aspect ratio toroidal coupling effects and in the kinetic analysis of the electron plasma transport induced by them. While the various toroidal geometry effects modify the numerical coefficients and radial structure of $\chi_e^{m/n}$ somewhat, they yield approximately the same qualitative behaviour for χ_e^{RMP} [40].

Precise tests of this magnetic flutter model of RMP-induced plasma transport will require using realistic flow-screened RMP-induced profiles $\delta\hat{B}_{\rho_{m/n}}^{\text{pl}}(x)$ in the evaluation of the general forms of the model predictions in (22), (15) and (18) for the edges of specific H-mode discharges. The needed RMP profiles in the edge plasma can be obtained from the extended MHD modeling codes. Such more precise evaluations might allow resolution of the apparently lower magnitude and weak q_{95} resonant sensitivity of the present model predictions. They would also facilitate exploration of triangularity, beta feedback control and other experimentally observed influences on the RMP-induced effects on the pedestal structure and ELM suppression.

The final question is: How do these RMP effects on plasma transport and consequently plasma profiles in the tokamak edge stabilise ELMs in these low collisionality DIII-D plasmas? The RMPs have been shown to mainly reduce the T_e gradient at the top of the pedestal with smaller decreases in the n_e and T_i gradients there. The relevant plasma profiles in the ideal MHD based P-B mode theory are the total plasma pressure gradient and bootstrap current profiles in the entire pedestal region. Apparently, the reductions in the plasma pressure gradient in the pedestal top region caused primarily by the RMP-induced reductions in the T_e gradient there are sufficient to move the edge plasma below the P-B stability boundary (see Fig. 6g in Ref. [10]).

The preceding discussion of RMP-flutter-induced plasma transport has been concerned with its effects on low collisionality DIII-D pedestals. The key effects are that: 1) (theoretically) while the radial transport can be very large near the rational surfaces and flatten the T_e profile there (see Fig. 7), the predicted average $\bar{\chi}_e^{\text{RMP}}$ is dominated by the minimum diffusivity midway between rational surfaces; and 2) (experimentally) the largest T_e profile changes occur in narrow resonant regions of q_{95} , apparently due (theoretically) to increased $\delta\hat{B}_{\rho m/n}^{\text{pl}}$ 10/3, 11/3 and 12/3 RMP responses near $\Psi_N \sim 0.95$.

The model's predictions are somewhat different for the higher collisionality RMP experiments in DIII-D [9, 41], NSTX [42] and AUG [43] where the electron collision frequency ν_e is typically an order of magnitude (or more) larger. This causes the various dissipative layer widths (δ , δ_{\parallel} , W_c^{Te}) to increase significantly. Most importantly, δ_{\parallel} becomes comparable to the distance between rational surfaces, which causes the RMP-induced parallel flow and heat flux responses to not be so large near rational surfaces and to overlap radially. In such high collisionality cases q_{95} resonance effects are less likely and the predicted RMP-induced electron thermal diffusivity scales roughly as $\chi_e^{\text{RMP}} \sim \nu_e L_S^2 \sum_{mn} [\delta\hat{B}_{\rho m/n}^{\text{vac}}/B_0]^2$. Also, the RMP-induced transport effects are probably not concentrated at the pedestal top but instead are likely to permeate throughout the entire plasma edge region. Detailed studies of these effects could contribute to an understanding of why ELMs can be resonantly suppressed in low collisionality DIII-D H-mode pedestals whereas ELMs are only mitigated (or changed into smaller, more frequent ELMs) in higher collisionality H-mode pedestals.

6. Summary

This paper has explored both experimentally and theoretically the effects of RMPs on plasma transport and the resulting plasma profiles in the edge of low-collisionality H-mode tokamak plasmas, such as those in DIII-D [10, 11, 12]. Experimentally, the main RMP effects are increases in the electron temperature gradient scale length L_{Te} at the top of the pedestal approximately proportional to the square of the RMP strength (I-coil current), with factor of about three smaller effects on the n_e gradient scale length.

Flow screening of RMP fields in the edge is predicted to be operative in these pedestals and reduce the possibility such fields could produce magnetic island overlap, stochastisation of the magnetic field there and resultant Rechester-Rosenbluth transport [17]. Thus, an alternative magnetic-flutter-type [16] model of RMP-induced plasma transport has been developed using a periodic cylinder screw pinch magnetic field model. The model predictions agree with some key aspects of the experimental data: the electron diffusivities scale with the square of the RMP strength and the increases in the electron thermal diffusivity are a factor of about three larger than the electron density diffusivity. However, the predicted magnitude of the electron thermal diffusivity is estimated to be roughly a factor of 3–8 smaller than the experimentally-inferred value. This simple model's predictions would be improved and could become larger if extended MHD modelling results for the flow-screened RMP-induced magnetic perturbations in

the plasma were used. Also, the $q_{95} \simeq 3.5$ resonance condition for RMP stabilisation of ELMs [11] is apparently not predicted by the simplified estimation procedure used here. However, it might be if the plasma response to the 10/3, 11/3 and/or 12/3 RMP components were larger and perhaps different from this model's analytic RMP-induced $\delta \hat{E}_{\rho m/n}^{\text{pl}}$ profile in flow-screened pedestal regions given by (3).

More work is needed on the development and testing of this new magnetic flutter model of RMP-induced plasma transport for both the low collisionality DIII-D pedestals [10, 11, 12] studied here and higher collisionality pedestals [9, 41, 42, 43]. A fully toroidal rather than cylindrical screw pinch model of flutter transport is being developed [40]. Realistic extended MHD modeling of flow-screening of RMP fields in the edge plasma needs to be developed for particular cases such as the 5.2 kA I-coil case discussed here and used to more precisely estimate the RMP-induced plasma transport in the edge region for both low and high collisionality pedestals. Also, studies are needed of the likely different RMP-induced plasma transport properties in the steep gradient region of low collisionality pedestals (where the n_e gradient is weakened by RMPs but the T_e gradient increases) to clarify why they are so different from those at pedestal top.

Acknowledgments

The authors are grateful to T.E. Evans, N.M. Ferraro, R.J. La Haye, M.J. Schaffer and many of their other colleagues in the DIII-D program for useful discussions about the many issues involved in RMP and flow screening effects on the magnetic field structure and plasma in the edge region of DIII-D. This research was supported by U.S. DoE grants DE-FG02-86ER53218 and DE-FG02-92ER54139 (UW-Madison), DE-FG02-05ER54809 and DE-FG02-07ER54917 (UCSD).

References

- [1] Hegna C.C., Connor J.W., Hastie R.J. and Wilson H.R. 1996 *Phys. Plasmas* **3** 584
- [2] Connor J.W., Hastie R.J., Wilson H.R. and Miller R.L. 1998 *Phys. Plasmas* **5** 2687
- [3] Wilson H.R., Snyder P.B., Huysmans G.T.A. and Miller R.L. 2002 *Phys. Plasmas* **9** 1277
- [4] Snyder P.B., Wilson H.R., Ferron J.R., Lao L.L., Leonard A.W., Osborne T.H., Turnbull A.D., Mossessian D., Murakami M., and Xu X.Q. 2002 *Phys. Plasmas* **9** 2037
- [5] Zohm H. 1996 *Plasma Phys. Control. Fusion* **38** 105
- [6] Suttrop W. 2000 *Plasma Phys. Control. Fusion* **42** A1
- [7] Loarte A. *et al* 2010 ITER ELM control requirements, ELM control schemes & required R & D, paper ITR/1-4 at the 23rd International Atomic Energy Agency (IAEA) Fusion Energy Conference (FEC), 11–16 October 2010, Daejeon, Korea. Available at http://www-pub.iaea.org/MTCD/Meetings/cn180_papers.asp
- [8] Aymar R., Chuyanov V.A., Huguet M., Shimomura Y., ITER Joint Central Team and ITER Home Teams 2001 *Nucl. Fusion* **41** 1301
- [9] Evans T.E. *et al* 2004 *Phys. Rev. Lett.* **92** 235003
- [10] Evans T.E. *et al* 2006 *Nature Physics* **2** 419
- [11] Evans T.E. *et al* 2008 *Nucl. Fusion* **48** 024002
- [12] Schmitz O. *et al* 2009 *Phys. Rev. Lett.* **103** 165005

- [13] Liu Y., Kirk A., and Nardon E. 2010 *Phys. Plasmas* **17** 122502
- [14] Chu M.S. *et al* 2011 *Nucl. Fusion* **51** 073036
- [15] Ferraro N.M. 2011 Calculations of two-fluid linear response to non-axisymmetric fields in tokamaks (2011 APS-DPP invited paper JI2.02, submitted to *Phys. Plasmas*)
- [16] Callen J.D. 1977 *Phys. Rev. Lett.* **39** 1540
- [17] Rechester A.B. and Rosenbluth M.N. 1978 *Phys. Rev. Lett.* **40** 38
- [18] Braginskii S.I. 1965 in *Reviews of Plasma Physics* edited by M.A. Leontovich (Consultants Bureau, New York, 1965) Vol. I, p 205
- [19] Callen J.D., Groebner R.J., Osborne T.H., Canik J.M., Owen L.W., Pankin A.Y., Rafiq T., Rognlien T.D. and Stacey W.M. 2010 *Nucl. Fusion* **50** 064004
- [20] Yu Q. and Günter S. 2009 *Nucl. Fusion* **49** 062001
- [21] Nardon E., Tamain T., Bécoulet M., Huysmans G. and Waelbroeck F.L. 2010 *Nucl. Fusion* 034002
- [22] Hazeltine R.D., Kotschenreuther M. and Morrison P.J. 1985 *Phys. Fluids* **28** 2466
- [23] Aydemir A.Y. 1992 *Phys. Fluids B* **4** 3469
- [24] Yu Q. and Günter S. 2011 *Nucl. Fusion* **51** 073030
- [25] Leconte M. and Diamond P.H. 2011 *Phys. Plasmas* **18** 082309
- [26] Mordijck S. 2011 Particle transport as a result of Resonant Magnetic Perturbations, Ph.D. Thesis, University of California-San Diego
- [27] Mordijck S., Doyle E.J., McKee G.R., Moyer R.A., Rhodes T.L., and Zeng L. 2012 Changes in particle transport as a result of Resonant Magnetic Perturbations in DIII-D (2011 APS-DPP invited paper CI2.02, submitted to *Phys. Plasmas*).
- [28] Osborne T.H., Snyder P.B., Burrell K.H., Evans T.E., Fenstermacher M.E., Leonard A.W., Moyer R.A., Schaffer M.J., and West W.P. 2008 *Journal of Physics: Conference Series* **123** 012014
- [29] Fitzpatrick R. 1995 *Phys. Plasmas* **2** 825
- [30] Chirikov B.V. 1978 *Sov. J. Plasma Phys.* **4** 289
- [31] Chirikov B.V. 1979 *Phys. Rep.* **52** 263
- [32] Fitzpatrick R. 1993 *Nucl. Fusion* **33** 1049
- [33] Hegna C.C. 2011 *Nucl. Fusion* **51** 113017
- [34] Cole A. and Fitzpatrick R. 2006 *Phys. Plasmas* **13** 032503
- [35] Bender C. and Orzag S. 1999 *Advanced Mathematical Methods for Scientists and Engineers* (Springer-Verlag, New York, 1999), p 383 ff
- [36] Hegna C.C. and Callen J.D. 1993 *Phys. Fluids B* **5** 1804
- [37] Chang Z. and Callen J.D. 1990 *Nucl. Fusion* **30** 219
- [38] Mordijck S., Moyer R.A., Kirk A., Tamain P., Temple D., McKee G.R. and Nardon E. 2011 *Plasma Phys. Control. Fusion* **53**, 122001
- [39] Callen J.D., Canik J.M. and Smith S.P. 2011 Pedestal Structure Model, report UW-CPTC 11-3R (submitted for publication, available via <http://www.cptc.wisc.edu>)
- [40] Callen J.D., Cole A.J. and Hegna C.C. 2011 Magnetic perturbation-induced plasma transport in H-mode pedestals, report UW-CPTC 11-15 (to be available via <http://www.cptc.wisc.edu>)
- [41] Moyer R.A. *et al* 2005 *Phys. Plasmas* **12** 056119
- [42] Canik J.M. *et al* 2011 *Phys. Plasmas* **18** 056118
- [43] Suttrop W. *et al* 2011 *Plasma Phys. Control. Fusion* **53** 124014